# Multi-species Ion Acceleration in 3D Magnetic Reconnection

Qile Zhang, Fan Guo, William Daughton, Hui Li, and Ari Le
*Los Alamos National Laboratory, Los Alamos, NM 87545, USA**

Tai Phan
*Physics Department and Space Sciences Laboratory,*
*University of California, Berkeley, Berkeley, CA 94720, USA*

Mihir Desai
*Southwest Research Institute, 6220 Culebra Road, San Antonio, TX 78238, USA and*
*Department of Physics and Astronomy, University of Texas at San Antonio, San Antonio, TX 78249, USA*

(Dated: October 11, 2022)

arXiv:2210.04113v1 [astro-ph.SR] 8 Oct 2022

**Magnetic reconnection drives explosive particle acceleration in a wide range of space and astrophysical applications. The energized particles often include multiple species (electrons, protons, heavy ions), but the underlying acceleration mechanism is poorly understood. In-situ observations of these minority heavy ions offer a more stringent test of acceleration mechanisms, but the multi-scale nature of reconnection hinders studies on heavy-ion acceleration. Here we employ hybrid simulations (fluid electron, kinetic ions) to capture 3D reconnection over an unprecedented range of scales. For the first time, our simulations demonstrate nonthermal acceleration of all available ion species into power-law spectra. The reconnection layers consist of fragmented kinking flux ropes as part of the reconnection-driven turbulence, which produces field-line chaos critical for accelerating all species. The upstream ion velocities influence the first Fermi reflection for injection. Then lower charge/mass species initiate Fermi acceleration at later times as they interact with growing flux ropes. The resulting spectra have similar power-law indices ($p \sim 4.5$), but different maximum energy/nucleon $\propto$ (charge/mass)$^{\alpha}$, with $\alpha \sim 0.6$ for low plasma $\beta$, and with $p$ and $\alpha$ increasing as $\beta$ approaches unity. These findings are consistent with observations at heliospheric current sheets and the magnetotail, and provide strong evidence suggesting Fermi acceleration as the dominant ion-acceleration mechanism.**

Magnetic reconnection has been widely recongized as a fast process for converting magnetic field energy into plasma bulk flows, plasma heating, and nonthermal particle acceleration. One of the major unsolved fundamental problems is the acceleration of energetic particles during magnetic reconnection, with broad applications to various magnetospheric, solar and astrophysical energetic phenomena. In-situ and remote observations have found numerous evidence for efficient particle acceleration during magnetic reconnection. Examples include energetic particles observed from solar flares [1, 2], switchbacks that potentially originate from interchange reconnection [3–5], near solar wind reconnecting current sheets [6], heliospheric current sheets (HCS) [7, 8] and the magnetotail [9–12]. Often, multiple species are observed, including electrons, protons, and multi-species heavier ions (of relatively minor abundance) [7, 11, 12]. These multi-species observations contain key information of the underlying acceleration process and can be a more stringent test of mechanisms such as the Fermi-acceleration theory [13–19] – where particles get accelerated by bouncing off contracting magnetic field lines repeatedly. The recent in-situ observations provide direct measurement of energetic ions near the reconnection layers, but the exact energization mechanisms are unknown. Parker Solar Probe observations near the reconnecting HCS find multi-species energetic ions with a scaling of maximum energy per nucleon $\varepsilon_{max} \propto (Q/M)^{\alpha}$ where $\alpha \sim 0.65 - 0.76$ ($M$ is the mass and $Q$ is the charge)[7]. Some Magnetospheric Multiscale Mission (MMS) observations at Earth's magnetotail suggest that the ion energization is ordered by energy per charge, which indicates $\alpha \sim 1$ [11, 12]. However, none of earlier reconnection theories can explain these new in-situ observations. For example, Drake et al. [20] suggested an inverse scaling on $Q/M$ ($\alpha < 0$) in the large-guide-field regime whereas HCS and the magnetotail feature low guide fields.

Fully kinetic simulations are the primary tools for modeling particle acceleration in collisionless magnetic reconnection, as it self-consistently includes key reconnection physics and feedback of energetic particles in the reconnection region. Till now, kinetic simulations of reconnection acceleration are still quite challenging due to the multiscale nature of the process. While several large-scale 3D fully kinetic simulations [19] have achieved efficient acceleration of electrons and protons, modeling nonthermal acceleration of heavier ions (up to Fe) is considerably more difficult as their gyromotion scales can be much larger ($\propto (Q/M)^{-1}$ at the same velocity).

Here, we use large-scale 3D hybrid-kinetic simulations (particle ions and fluid electrons) to investigate the multi-species ion acceleration in reconnection. Despite the ap-

proximate fluid description employed for the electrons, large-scale hybrid simulations have demonstrated good agreement for the reconnection rate in comparisons with fully kinetic simulations [21–23]. Since the hybrid simulations do not need to resolve the electron inertial scale, they are about $(d_H/d_e) = (m_H/m_e)^{1/2}$ times more computationally cost efficient in each dimension than fully kinetic simulations. Here $d_H$ and $d_e$ are the inertial length of protons and electrons, $m_H$ and $m_e$ are the mass of protons and electrons. Therefore they enable much larger domains to capture the essential physics of heavy ion acceleration. Our hybrid simulations, for the first time, achieved efficient acceleration of all ion species (up to Fe) into nonthermal power-law energy spectra. In the simulations, we find that the 3D reconnection layers consist of fragmented kinking flux ropes across different scales, which are growing in width and length over time, as a distinct component of the reconnection-driven turbulence. Similar strong magnetic fluctuations have also been observed in magnetotail reconnection [9, 10]. This 3D dynamics plays a critical role in the particle acceleration for all species. This is due to self-generated field line chaos, which prevents the artificial trapping of energetic particles within flux ropes (commonly observed in 2D simulations) and allows efficient Fermi acceleration [19]. Different ions are pre-accelerated from their initial energy into nonthermal energies by bouncing off the Alfvénic outflows at reconnection exhausts (injection). The injection process leads to low-energy shoulders in the energy spectra, which controls the nonthermal energy contents. At higher energy, all particle species undergo a universal Fermi acceleration process to form power-law energy spectra with similar indices ($p \sim 4.5$) regardless the gyroradii of the ions. However, the onset times of Fermi acceleration for different species depend on when they are magnetized as the magnetic flux ropes and neighboring exhausts grow, due to different gyroradii. As a result, their maximum energy per nucleon follows a scaling of $\varepsilon_{max} \propto (Q/M)^{\alpha}$ where $\alpha \sim 0.6$ for low plasma $\beta$. $p$ and $\alpha$ increase as $\beta$ approaches unity. These results agree reasonably with the HCS and magnetotail observations [7, 11, 12], suggesting that these observations can be the natural consequences of reconnection.

We use the Hybrid-VPIC code [24] that evolves ions of different species as nonrelativistic kinetic particles and electrons as an adiabatic fluid, which is coupled with Ohm's law (with hyper-resistivity and resistivity to break the electron frozen-in condition), Ampere's law (without Maxwell's displacement current) and Faraday's law. The 3D hybrid simulations start from two identical current sheets with periodic boundaries in all spatial dimensions. The current sheets have a force-free profile

$$\begin{aligned}\mathbf{B} =& B_0(\tanh((z-0.25L_z)/\lambda) \\ &- \tanh((z-0.75L_z)/\lambda) - 1)\mathbf{e_x} \\ &+ (B_0^2(\mathrm{sech}^2((z-0.25L_z)/\lambda) \\ &+ \mathrm{sech}^2((z-0.75L_z)/\lambda)) + B_g^2)^{\frac{1}{2}}\mathbf{e_y}\end{aligned} \tag{1}$$

with uniform density and temperature. $B_0$ is the reconnecting field, $B_g$ is the guide field, $L_z$ is the domain size in $z$ and $\lambda$ is the half thickness of the sheet set to be one proton inertial length $d_H$. The guide field $b_g = B_g/B_0 = 0.1$ (corresponding to a magnetic shear angle 169° very typical in HCS observations [8, 25]), which represents in general the low guide field regime in HCS and the magnetotail [26–28]. We include several ion species ${}^{1}\mathrm{H}^{+}$, ${}^{4}\mathrm{He}^{2+}$, ${}^{3}\mathrm{He}^{2+}$, ${}^{16}\mathrm{O}^{7+}$, ${}^{56}\mathrm{Fe}^{14+}$, with abundance 95%, 5%, 0.1%, 0.1%, 0.1% respectively. We perform three runs with different initial temperatures $T_i = T_e = 0.04, 0.09, 0.25 m_H V_A^2$, where $V_A = B_0/\sqrt{4\pi n_H m_H}$ is the Alfvén speed with proton density $n_H$, so proton $\beta_H = 0.08, 0.18, 0.5$ respectively. We analyze the $\beta_H = 0.18$ run by default and use others for comparison. We will only focus on one of the current sheets in the following. Further details of the simulations are given in the Methods section. Our simulations are relevant for multi-X-line collisionless reconnection, as well as a hierarchy of collisional plasmoids in the initially thick current sheet that may develop kinetic-scale current sheets to trigger collisionless reconnection [29–33].

**Reconnection Current Sheet with 3D Fragmented Kinking Flux Ropes**

Figure 1(a)-(d) shows $B_z$ in the $x-y$ plane in the center of one current sheet at different times. The current sheet (around $x = 675d_H$) consists of fragmented magnetic flux ropes, resulting from kink instability of tearing-mode-generated flux ropes. As reconnection proceeds, these fragmented kinking flux ropes are still growing over time both in width and length, while they advect along with the large bidirectional reconnection outflows in the $x$ direction. We visualize these flux ropes in 3D using proton density at $t\Omega_{cH} = 600$ in Figure 1(e-f) from different perspectives. Panel (e) has the same perspective as panel (c) so flux ropes in (e) can be directly compared to the corresponding ones in (c). Panel (f) emphasizes that flux ropes exist over a range of scales, with two sub-panels showing magnified views at different scales. One flux rope is newly born from the reconnection layer (green box), and the other has grown to occupy a sizeable fraction of the simulation domain. This flux-rope kink instability produces chaotic field lines [19] that can diverge quickly and connect outside of the flux ropes [34, 35], which enables particles transport out of flux ropes and further acceleration at the adjacent reconnection exhausts (see also Extended Data Figure E1). As we will also demonstrate, the acceleration physics is influenced by the ion gyroradii

interacting with the different scales of this reconnection-driven turbulence.

**Acceleration of Different Ions Species**

Figure 2(a) shows the particle spectra of different ion species at $t\Omega_{cH} = 1800$ normalized by abundance, as a function of their energy per nucleon $\varepsilon$. For the first time, the simulation shows that all ion species are accelerated into power-law energy spectra with similar indices around $p = 4.5$, suggesting a universal process of ion acceleration across different species. Moreover, each species develops a shoulder feature in the energy spectra, which differentiates the power laws from the heated portion. These low energy bounds of the power laws for different species are similar, indicating a similar injection process for all species (the difference will be discussed below). We obtain the power-law high-energy cutoffs of $\varepsilon_{max}$ for different species (details in the Methods section) and show the relative values in Figure 2(b), where different species follows a fitted scaling of $(Q/M)^{\alpha}$ ($\alpha \sim 0.68$). A simulation with somewhat lower $\beta_H = 0.08$ produces similar $p \sim 4.0$ and $\alpha \sim 0.61$. In contrast, a simulation with somewhat higher $\beta_H = 0.5$ approaching unity produces $p \sim 6.3$ and $\alpha \sim 1.18$. Our simulation results agree reasonably with the HCS observations [7] where upstream $\beta_H \sim 0.2$, $\alpha \sim 0.65 - 0.76$ and $p \sim 4 - 6$ (see Figure 2(b) $\alpha = 0.7$ as a reference line). In MMS observations [11, 12] where upstream $\beta_H$ (usually $< 1$) is difficult to measure precisely, the inferred exponents ($\alpha \sim 1$ and $p \sim 5 - 6$) are comparable to simulation results (see Figure 2(b) $\alpha = 1$). The agreement with observations suggests reconnection as the source of particle acceleration. We also performed corresponding 2D simulations and find less efficient acceleration and softer spectra than 3D (see Extended Data Figure E2), showing that 3D effects are critical for particle acceleration of all species. The time evolution of $\varepsilon_{max}$ for different species is shown in Figure 2(c), which features a common evolution pattern across different species. Different $\varepsilon_{max}$ first increase to a certain value at the order of $m_H V_A^2$ close to the shoulders in Figure 2(a), representing an injection process. Later on, different species start increasing at a similar slope following about $t^{0.75}$, again indicating a universal acceleration process. Intriguingly, the transition between the injection and later acceleration has different timing depending on the species, leading to different maximum energy.

**Particle Injection and Acceleration Mechanisms**

We find that different ions are commonly accelerated by a Fermi acceleration process at contracting field lines, which produces indices $p \sim 4.5$ and acceleration $\varepsilon \propto t^{0.75}$ for protons and heavier ions up to Fe. This is similar to the earlier prediction from Fermi acceleration for protons and electrons in the low-$\beta$ limit [19]. While heavier ions have larger gyroradii, the Fermi process for them still operates, suggesting that this mechanism can apply at a scale larger than the gyromotion and can be applied to a broad range of different ion species. We also find that a higher initial $\beta$ approaching unity can steepen the power laws by weakening field-line contraction associated with Fermi acceleration, as explained in the following. On one hand, the high initial pressure due to high initial $\beta$ hinders flux-rope compression (found in our simulations) that leads to field-line contraction [17]. On the other hand, this high initial pressure enables Fermi acceleration (proportional to energy) to boost pressure anisotropy (parallel pressure minus perpendicular pressure) to become comparable to magnetic pressure, which weakens the firehose parameter (found in our simulations) and thus field-line tension that drives field-line contraction [36].

While the Fermi acceleration gives the same acceleration rate for all species (Figure 2(c)), their injection processes have some noticeable difference. We find that all ion species can be injected through a single Fermi reflection at the exhausts, but are affected by their individual initial thermal velocities (lower for heavier ions). Taking the typical speed in the exhausts measured in the simulation (with $\beta = 0.18$) $V_0 \sim 0.6V_A$, we can estimate the injection energy that a particle can reach by a Fermi reflection

$$\varepsilon_{inj} \sim 0.5 m_H (2V_0 + 2V_{th})^2 = 2m_H (V_0 + V_{th})^2 \qquad (2)$$

where the initial thermal speed $V_{th} = \sqrt{T_0/M}$. This theoretical estimate agrees approximately with the shoulders for different species in Figure 2(a) (determined at a level $10^7$), as demonstrated in Figure 2(d).

Interestingly, lower Q/M ions have later onset time of Fermi acceleration, which will be explained below. Note that there is an short-term energy increase before $t\Omega_{ci} = 300$ for all species distinct from Fermi acceleration, more apparent for heavy ions. This is because a far-downstream portion (hundreds of $d_H$ from the x-line) of the large elongated exhausts formed at this early time reaches a somewhat higher exhaust speed ($\sim 0.8V_A$). At later time after the exhausts break up into flux ropes, this effect vanishes and gets overwhelmed by Fermi acceleration. The later onset of Fermi acceleration for lower Q/M ions is caused by their larger gyroradii after injection, so that they get magnetized at later times when magnetic flux ropes and their adjacent exhausts grow large enough. We demonstrate this in Figure 3 by showing the energetic particles density (normalized by their initial density) beyond their injection energies (Equation 2) at two different times (vertical dot-dash lines in Figure 2(c)) in the $x - z$ plane, zooming into the region filled with magnetic flux ropes ($x \in [490d_H, 860d_H]$). At $t\Omega_{cH} = 300$, with relatively small magnetic flux ropes ($\sim 5d_H$ in $z$), protons (post-injection gyroradius $\rho_H \sim 1.4$ taking $\varepsilon_{inj} \sim 1$) have already started Fermi acceleration for some time with many particles beyond the injection energy, while $^3$He just started, and most Oxygens (post-injection $\rho_O \sim 3.2$)

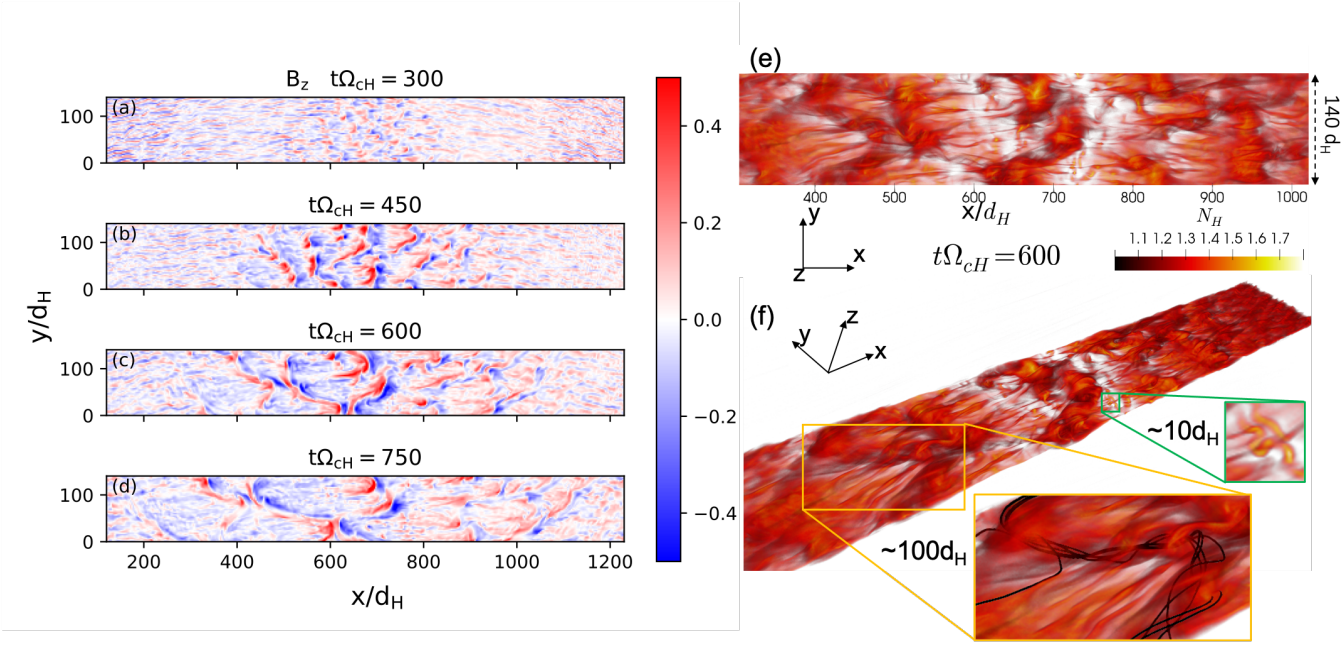


FIG. 1. **Fragmented kinking flux ropes in 3D turbulent reconnection.** (a)-(d) Magnetic field $B_z$ in the $x-y$ plane in the center of the current sheet ($z = 168d_H$) at different times to show the evolution of growing fragmented kinking magnetic flux ropes. (e-f) Volume rendering of flux ropes in 3D using proton density at $t\Omega_{cH} = 600$ from different perspectives, with two magnified windows ($\sim 10d_H$ and $\sim 100d_H$) showing example kinking flux ropes of vastly different scales in (f). In the $\sim 100d_H$ window, some example field lines around the flux rope better visualize the flux rope dynamics.

have not been through Fermi acceleration. In contrast, at $t\Omega_{cH} = 450$ the magnetic flux ropes become larger ($\sim 10d_H$ in $z$) and all ion species are magnetized after injection, allowing continuous Fermi acceleration.

Based on the simulation results, we perform the following scaling study to further elucidate this mechanism. When $\beta \ll 1$, the injection energy per nucleon $\varepsilon_{inj} \sim m_H V_A^2$ are similar for different species. Thus, the gyroradius after injection scales as $\rho_x \propto (Q_x/M_x)^{-1}$ for a species $x$. Assuming flux ropes grow linearly over time, the starting time of magnetization and Fermi acceleration scales as $t_0 \propto (Q_x/M_x)^{-1}$. We set

$$\varepsilon_{max,x} \sim C_x t^{\gamma} \tag{3}$$

during Fermi acceleration at the reconnection layer (lasting for about one Alfvén crossing time $L_x/V_A$ proportional to the domain size) where $C_x$ is a species-specific constant. Since $\varepsilon_{max} = \varepsilon_{inj}$ at $t = t_0$, we get

$$\varepsilon_{max,x}/\varepsilon_{max,H} \propto C_x \propto (Q_x/M_x)^{\gamma}. \tag{4}$$

Since $\varepsilon_{max,x}/\varepsilon_{max,H} \propto (Q_x/M_x)^{\alpha}$, we get $\alpha \sim \gamma$. Given $\gamma \sim 0.75$ during acceleration in the current simulation, it roughly agrees with $\alpha \sim 0.6$ in Figure 2(b). A higher initial $\beta$ of order unity will introduce corrections to these results due to higher $\varepsilon_{inj}$ for higher $V_{th} = \sqrt{T_0/M}$ ions, eventually increasing the relative difference of $\varepsilon_{max}$ and therefore $\alpha$. Note that Equation 3 implies maximum gyroradius as a function of time $\rho_{max,x} \propto \sqrt{\varepsilon_{max,x}} \propto t^{\gamma/2} \sim t^{0.38}$ which grows over time much slower than the flux ropes ($\propto t$), so the highest energy particles can stay magnetized for Fermi acceleration.

In this paper, our 3D hybrid simulations demonstrate simultaneous nonthermal acceleration of all available ion species (up to Fe) in magnetic reconnection. With these simulations, we have uncovered the 3D turbulent dynamics and the fundamental mechanisms of particle injection and acceleration for multi-species ion acceleration in reconnection, with strong implications to space and astrophysics. Our prediction of exponents $(p, \alpha)$ can naturally explain the current observations near HCS and the magnetotail with a low guide field. The remote sources like interchange reconnection and solar flares on the Sun will be further explored, where parameters and geometry are less constrained. Our hybrid simulations do not take into account the electron acceleration process (only adiabatic heating) and electron pressure anisotropy, which can potentially influence magnetic tension and the energy release process. However, previous researches suggest that electrons have less energy gain and pressure anisotropy than protons in reconnection [19, 37–42] due to weaker gain from Fermi reflection. The 3D flux-rope dynamics and the dependence of features (such as $p, \alpha, \varepsilon_{inj}$) on parameters can be compared in details with new spacecraft measurements in the future, which is critical for understanding particle acceleration in reconnection.

**Methods**

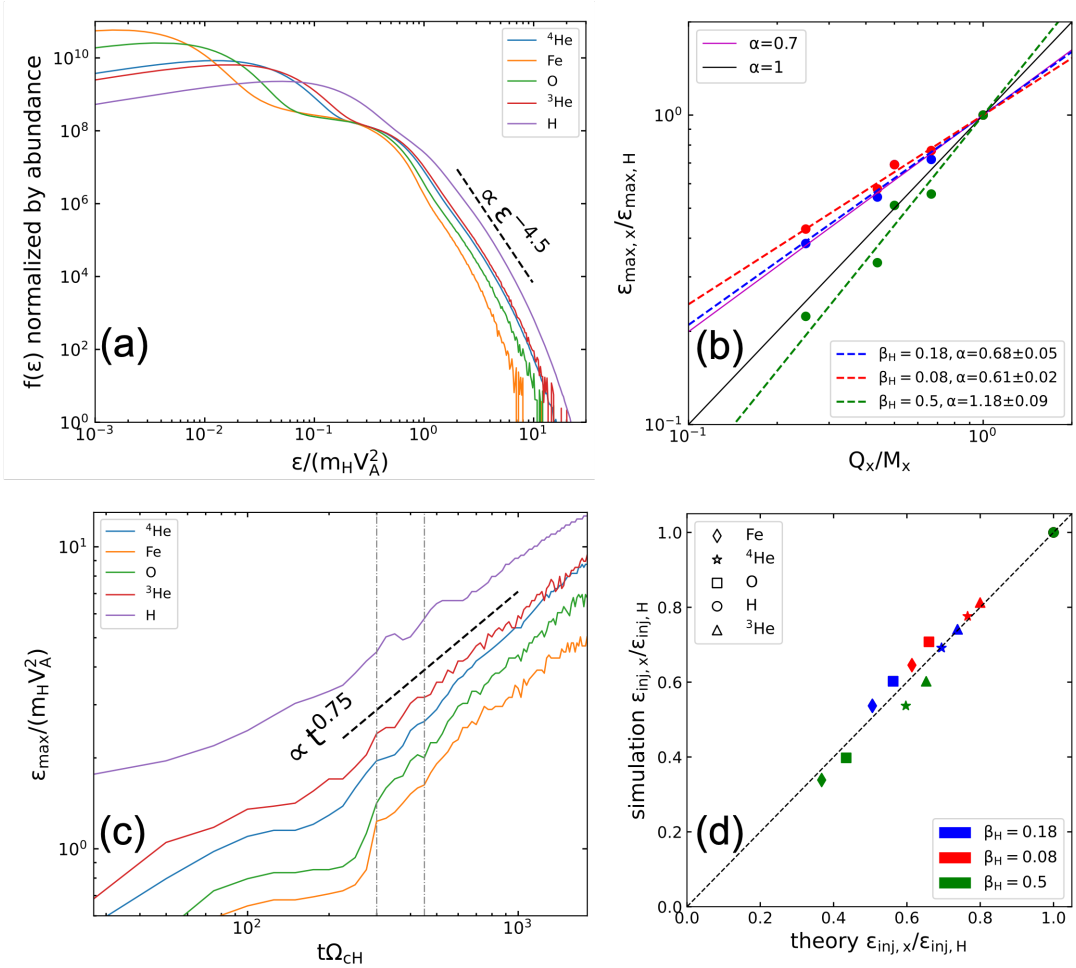


FIG. 2. **Injection and nonthermal acceleration of different ion species.** (a) final particle energy spectra normalized by the total abundance of each species versus particle energy per nucleon $\varepsilon$. (b) maximum energy per nucleon $\varepsilon_{max}$ for each species normalized by that of Hydrogen versus charge-to-mass ratio for each species, shown for three cases of different $\beta_H$. The red, blue and green dash lines fit $(Q_x/M_x)^\alpha$ for different cases. Two solid reference lines $\alpha = 0.7, 1.0$ indicate the observations. (c) $\varepsilon_{max}$ versus time for different species. Two vertical dot-dash lines indicate two times evaluated in Figure 3. (d) theoretical predictions of the injection energies (shoulders) for different species normalized by that of Hydrogen versus those obtained in simulations.

The simulation domain size $L_x \times L_y \times L_z = 1350 \times 140.4 \times 672 d_H^3$, with grid size $\Delta x = \Delta y = \Delta z = 0.6 d_H$ and 800 protons per cell. The length of the simulation domain in the y direction is sufficient for resolving the $m = 1$ flux-rope kink mode for efficient nonthermal particle acceleration [19]. Small long-wavelength perturbations are included to initiate reconnection at both current sheets. To limit the influence of periodic boundaries, the simulations terminate around 1.3 Alfvén crossing time $L_x/V_A$, during which only about 1/3 of the upstream magnetic flux is reconnected and two current sheets do not affect each other. In a real system with open boundaries, reconnection can keep going on, so the flux-rope dynamics in our simulations will occur repeatedly. The power-law high-energy cutoffs in Figure 2 are determined by the higher energies at which the spectra deviates from the fitted power-laws by $e \sim 2.718$. Before this procedure, the nonthermal spectra are presmoothed using non-increasing isotonic regression (with scikit-learn's [43] IsotonicRegression module). The $\varepsilon_{max}$ ratios in Figure 2(b) have been averaged over 6 time moments (separated by $25\Omega_{cH}^{-1}$) before the end of the simulations ($t\Omega_{cH} = 1800$), to handle fluctuations seen in Figure 2(c).

**Extended Data**

See Figure E1 and Figure E2.

**Acknowledgment.**— We gratefully acknowledge the helpful discussions in the SolFER DRIVE Science Center collaboration. We also acknowledge technical support from Xiaocan Li at Dartmouth College, and Adam Stanier at Los Alamos National Laboratory. Q.Z, F.G., W.D. and H.L. acknowl-

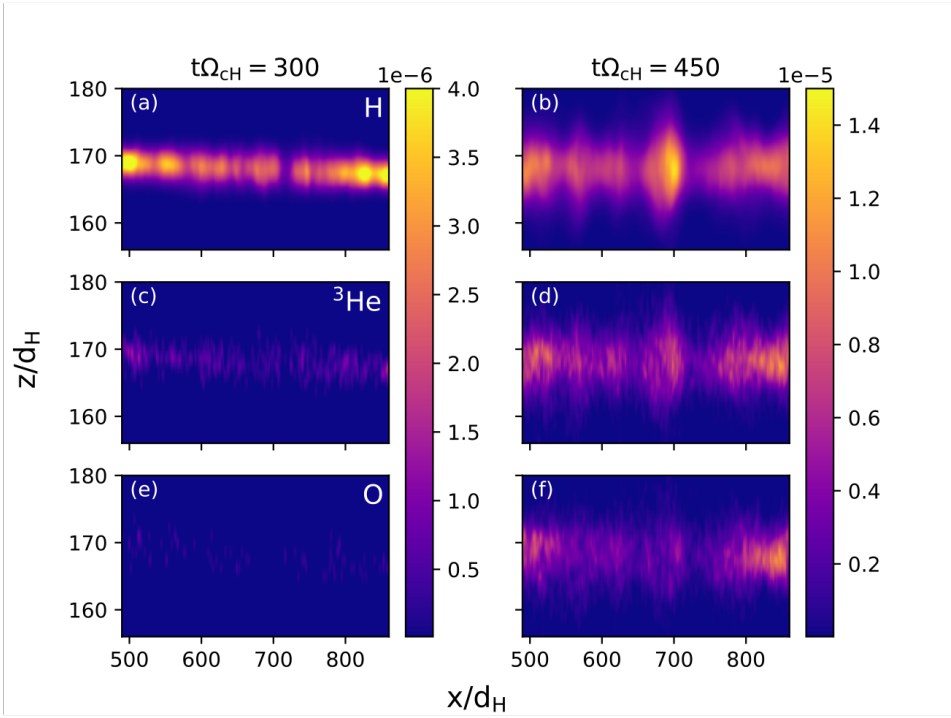


FIG. 3. **Different ion species are magnetized and accelerated at different times.** The density of energetic particles above injection energy for different species (H - top, $^3$He - middle, O - bottom) in the $x-z$ plane (averaged over $y$) in the region full of magnetic islands at two different times.

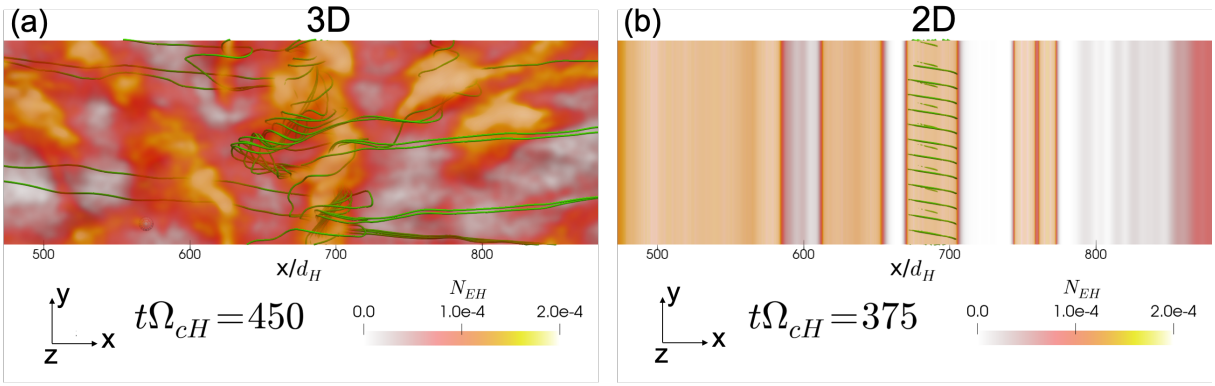


FIG. E1. **3D field-line chaos detraps particles from flux ropes.** (a) energetic proton density $N_{EH}$ in the energy range $[3.4m_H V_A^2, 6.8m_H V_A^2]$ at $t\Omega_{cH} = 450$ in the 3D simulation with $\beta_H = 0.18$. This has the same perspective as Figure 1(b) for direct comparison. We also show 17 sample field lines starting from the core of a flux rope at x=690 near the bottom. The field lines become chaotic and connect outside of the flux rope and also to other fragmented flux ropes, enabling particles to spread throughout the reconnection layer for efficient acceleration. (b) in comparison, a similar demonstration for the 2D counterpart without variation in $y$ at $t\Omega_{cH} = 375$ with an similar amount of magnetic flux reconnected as panel (a). The field lines and energetic particles are mostly confined within the flux rope, hindering efficient acceleration.

edge the support from Los Alamos National Laboratory through the LDRD program and its Center for Space and Earth Science (CSES), DOE OFES, and NASA programs through grant NNH17AE68I, 80HQTR20T0073, 80NSSC20K0627, 80HQTR21T0103 and 80HQTR21T0005, and through Astrophysical Theory Program. The simulations used resources provided by the Los Alamos National Laboratory Institutional Computing Program, the National Energy Research Scientific Computing Center (NERSC) and the Texas Advanced Computing Center (TACC).

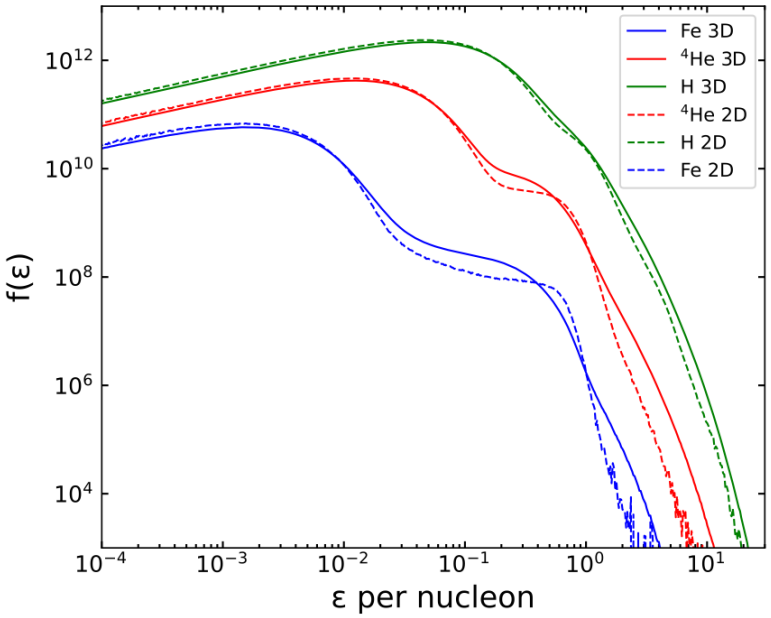


FIG. E2. **3D simulations have more efficient acceleration than 2D for all ion species.** Ion energy spectra in the 3D simulation ($\beta_H = 0.18$) at $t\Omega_{cH} = 1800$ in comparison to the 2D counterpart at the time when a similar amount of magnetic flux is reconnected. The 2D simulation are normalized to have the same number of particles as 3D. The spectra of different species are not normalized by abundance (unlike Figure 2(a)) so major and minor ions are separated in scales from each other.

* qlzhang@lanl.gov


[1] Mason, G. M., Ho, G. C., Allen, R. C., Rodríguez-Pacheco, J., Wimmer-Schweingruber, R. F., Bucík, R., Gómez-Herrero, R., Lario, D., von Forstner, J. L. F., Andrews, G. B., Berger, L., Cernuda, I., Espinosa Lara, F., Lees, W. J., Martin, C., Pacheco, D., Prieto, M., Sánchez-Prieto, S., Hayes, J. R., Schlemm, C. E., Seifert, H., and Tyagi, K., 3he-rich solar energetic particle events observed on the first perihelion pass of solar orbiter, A&A **656**, L1 (2021).

[2] C. M. S. Cohen *et al.*, Parker Solar Probe Observations of He/H Abundance Variations in SEP Events inside 0.5 AU, A&A 10.1051/0004-6361/202039299 (2020).

[3] S. D. Bale, T. S. Horbury, M. Velli, M. I. Desai, J. S. Halekas, M. D. McManus, O. Panasenco, S. T. Badman, T. A. Bowen, B. D. G. Chandran, J. F. Drake, J. C. Kasper, R. Laker, A. Mallet, L. Matteini, T. D. Phan, N. E. Raouafi, J. Squire, L. D. Woodham, and T. Woolley, A Solar Source of Alfvénic Magnetic Field Switchbacks: In Situ Remnants of Magnetic Funnels on Supergranulation Scales, ApJ **923**, 174 (2021), arXiv:2109.01069 [astro-ph.SR].

[4] S. D. Bale, J. F. Drake, M. D. McManus, M. I. Desai, S. T. Badman, D. E. Larson, M. Swisdak, N. E. Raouafi, T. Phan, M. Velli, D. J. McComas, C. M. S. Cohen, D. Mitchell, O. Panasenco, and J. C. Kasper, Interchange reconnection within coronal holes powers the fast solar wind, arXiv e-prints , arXiv:2208.07932 (2022), arXiv:2208.07932 [astro-ph.SR].

[5] J. F. Drake, O. Agapitov, M. Swisdak, S. T. Badman, S. D. Bale, T. S. Horbury, J. C. Kasper, R. J. MacDowall, F. S. Mozer, T. D. Phan, M. Pulupa, A. Szabo, and M. Velli, Switchbacks as signatures of magnetic flux ropes generated by interchange reconnection in the corona, A&A **650**, A2 (2021), arXiv:2009.05645 [astro-ph.SR].

[6] O. V. Khabarova and G. P. Zank, Energetic Particles of keV-MeV Energies Observed near Reconnecting Current Sheets at 1 au, ApJ **843**, 4 (2017).

[7] M. I. Desai, D. G. Mitchell, D. J. McComas, J. F. Drake, T. Phan, J. R. Szalay, E. C. Roelof, J. Giacalone, M. E. Hill, E. R. Christian, N. A. Schwadron, R. L. McNutt, M. E. Wiedenbeck, C. Joyce, C. M. S. Cohen, A. J. Davis, S. M. Krimigis, R. A. Leske, W. H. Matthaeus, O. Malandraki, R. A. Mewaldt, A. Labrador, E. C. Stone, S. D. Bale, J. Verniero, A. Rahmati, P. Whittlesey, R. Livi, D. Larson, M. Pulupa, R. J. MacDowall, J. T. Niehof, J. C. Kasper, and T. S. Horbury, Suprathermal Ion Energy Spectra and Anisotropies near the Heliospheric Current Sheet Crossing Observed by the Parker Solar Probe during Encounter 7, ApJ **927**, 62 (2022), arXiv:2111.00954 [astro-ph.SR].

[8] T. D. Phan, J. L. Verniero, D. Larson, B. Lavraud, J. F. Drake, M. Øieroset, J. P. Eastwood, S. D. Bale, R. Livi, J. S. Halekas, P. L. Whittlesey, A. Rahmati, D. Stansby, M. Pulupa, R. J. MacDowall, P. A. Szabo, A. Koval, M. Desai, S. A. Fuselier, M. Velli, M. Hesse, P. S. Pyakurel, K. Maheshwari, J. C. Kasper, J. M. Stevens, A. W. Case, and N. E. Raouafi, Parker So-

lar Probe Observations of Solar Wind Energetic Proton Beams Produced by Magnetic Reconnection in the Near-Sun Heliospheric Current Sheet, Geophys. Res. Lett. **49**, e96986 (2022).

[9] R. E. Ergun, K. A. Goodrich, F. D. Wilder, N. Ahmadi, J. C. Holmes, S. Eriksson, J. E. Stawarz, R. Nakamura, K. J. Genestreti, M. Hesse, J. L. Burch, R. B. Torbert, T. D. Phan, S. J. Schwartz, J. P. Eastwood, R. J. Strangeway, O. Le Contel, C. T. Russell, M. R. Argall, P. A. Lindqvist, L. J. Chen, P. A. Cassak, B. L. Giles, J. C. Dorelli, D. Gershman, T. W. Leonard, B. Lavraud, A. Retino, W. Matthaeus, and A. Vaivads, Magnetic Reconnection, Turbulence, and Particle Acceleration: Observations in the Earth's Magnetotail, Geophys. Res. Lett. **45**, 3338 (2018).

[10] R. E. Ergun, N. Ahmadi, L. Kromyda, S. J. Schwartz, A. Chasapis, S. Hoilijoki, F. D. Wilder, J. E. Stawarz, K. A. Goodrich, D. L. Turner, I. J. Cohen, S. T. Bingham, J. C. Holmes, R. Nakamura, F. Pucci, R. B. Torbert, J. L. Burch, P. A. Lindqvist, R. J. Strangeway, O. Le Contel, and B. L. Giles, Observations of Particle Acceleration in Magnetic Reconnection-driven Turbulence, ApJ **898**, 154 (2020).

[11] S. T. Bingham, I. J. Cohen, B. H. Mauk, D. L. Turner, D. G. Mitchell, S. K. Vines, S. A. Fuselier, R. B. Torbert, and J. L. Burch, Charge-State-Dependent Energization of Suprathermal Ions During Substorm Injections Observed by MMS in the Magnetotail, Journal of Geophysical Research (Space Physics) **125**, e28144 (2020).

[12] L. Richard, Y. V. Khotyaintsev, D. B. Graham, A. Vaivads, R. Nikoukar, I. J. Cohen, D. L. Turner, S. A. Fuselier, and C. T. Russell, Proton and helium ion acceleration at magnetotail plasma jets, Journal of Geophysical Research: Space Physics **127**, e2022JA030430 (2022), e2022JA030430 2022JA030430.

[13] J. F. Drake, M. Swisdak, H. Che, and M. A. Shay, Electron Acceleration from Contracting Magnetic Islands during Reconnection, Nature **443**, 553 (2006).

[14] J. T. Dahlin, J. F. Drake, and M. Swisdak, The Mechanisms of Electron Heating and Acceleration during Magnetic Reconnection, Phys. Plasmas **21**, 092304 (2014).

[15] J. T. Dahlin, J. F. Drake, and M. Swisdak, The Role of Three-dimensional Transport in Driving Enhanced Electron Acceleration during Magnetic Reconnection, Phys. Plasmas **24**, 92110 (2017).

[16] X. Li, F. Guo, H. Li, and G. Li, Particle Acceleration during Magnetic Reconnection in a Low-beta Plasma, ApJ **843**, 21 (2017).

[17] X. Li, F. Guo, H. Li, and J. Birn, The Roles of Fluid Compression and Shear in Electron Energization during Magnetic Reconnection, ApJ **855**, 80 (2018), arXiv:1801.02255 [physics.plasm-ph].

[18] X. Li, F. Guo, H. Li, A. Stanier, and P. Kilian, Formation of Power-law Electron Energy Spectra in Three-dimensional Low-$\beta$ Magnetic Reconnection, ApJ **884**, 118 (2019), arXiv:1909.01911 [astro-ph.SR].

[19] Q. Zhang, F. Guo, W. Daughton, H. Li, and X. Li, Efficient nonthermal ion and electron acceleration enabled by the flux-rope kink instability in 3d nonrelativistic magnetic reconnection, Phys. Rev. Lett. **127**, 185101 (2021).

[20] J. F. Drake, P. A. Cassak, M. A. Shay, M. Swisdak, and E. Quataert, a Magnetic Reconnection Mechanism for Ion Acceleration and Abundance Enhancements in Impulsive Flares, ApJ **700**, L16 (2009).

[21] A. Stanier, W. Daughton, L. Chacón, H. Karimabadi, J. Ng, Y.-M. Huang, A. Hakim, and A. Bhattacharjee, Role of ion kinetic physics in the interaction of magnetic flux ropes, Phys. Rev. Lett. **115**, 175004 (2015).

[22] A. Stanier, W. Daughton, A. N. Simakov, L. Chacón, A. Le, H. Karimabadi, J. Ng, and A. Bhattacharjee, The role of guide field in magnetic reconnection driven by island coalescence, Physics of Plasmas **24**, 022124 (2017), https://doi.org/10.1063/1.4976712.

[23] A. Le, W. Daughton, H. Karimabadi, and J. Egedal, Hybrid simulations of magnetic reconnection with kinetic ions and fluid electron pressure anisotropy, Physics of Plasmas **23**, 032114 (2016), https://doi.org/10.1063/1.4943893.

[24] A. Le, D. Winske, A. Stanier, W. Daughton, M. Cowee, B. Wetherton, and F. Guo, Astrophysical Explosions Revisited: Collisionless Coupling of Debris to Magnetized Plasma, Journal of Geophysical Research (Space Physics) **126**, e29125 (2021), arXiv:2109.00583 [physics.plasm-ph].

[25] T. D. Phan, B. Lavraud, J. S. Halekas, M. Øieroset, J. F. Drake, J. P. Eastwood, M. A. Shay, P. S. Pyakurel, S. D. Bale, D. Larson, R. Livi, P. L. Whittlesey, A. Rahmati, M. Pulupa, M. D. McManus, J. L. Verniero, J. W. Bonnell, N. A. Schwadron, M. Stevens, A. W. Case, J. C. Kasper, R. J. MacDowall, P. A. Szabo, A. Koval, K. E. Korreck, T. Dudok de Wit, D. Malaspina, K. Goetz, and P. R. Harvey, Prevalence of magnetic reconnection in the near-Sun heliospheric current sheet, A&A **650**, A13 (2021).

[26] R. B. Torbert, J. L. Burch, T. D. Phan, M. Hesse, M. R. Argall, J. Shuster, R. E. Ergun, L. Alm, R. Nakamura, K. J. Genestreti, D. J. Gershman, W. R. Paterson, D. L. Turner, I. Cohen, B. L. Giles, C. J. Pollock, S. Wang, L. J. Chen, J. E. Stawarz, J. P. Eastwood, K. J. Hwang, C. Farrugia, I. Dors, H. Vaith, C. Mouikis, A. Ardakani, B. H. Mauk, S. A. Fuselier, C. T. Russell, R. J. Strangeway, T. E. Moore, J. F. Drake, M. A. Shay, Y. V. Khotyaintsev, P. A. Lindqvist, W. Baumjohann, F. D. Wilder, N. Ahmadi, J. C. Dorelli, L. A. Avanov, M. Oka, D. N. Baker, J. F. Fennell, J. B. Blake, A. N. Jaynes, O. Le Contel, S. M. Petrinec, B. Lavraud, and Y. Saito, Electron-scale dynamics of the diffusion region during symmetric magnetic reconnection in space, Science **362**, 1391 (2018), arXiv:1809.06932 [physics.space-ph].

[27] M. Øieroset, T. D. Phan, M. Fujimoto, R. P. Lin, and R. P. Lepping, In situ detection of collisionless reconnection in the Earth's magnetotail, Nature **412**, 414 (2001).

[28] L. J. Chen, S. Wang, M. Hesse, R. E. Ergun, T. Moore, B. Giles, N. Bessho, C. Russell, J. Burch, R. B. Torbert, K. J. Genestreti, W. Paterson, C. Pollock, B. Lavraud, O. Le Contel, R. Strangeway, Y. V. Khotyaintsev, and P. A. Lindqvist, Electron Diffusion Regions in Magnetotail Reconnection Under Varying Guide Fields, Geophys. Res. Lett. **46**, 6230 (2019).

[29] K. Shibata and S. Tanuma, Plasmoid-induced-reconnection and fractal reconnection, Earth, Planets, and Space **53**, 473 (2001), arXiv:astro-ph/0101008 [astro-ph].

[30] L. Comisso, M. Lingam, Y. M. Huang, and A. Bhattacharjee, Plasmoid Instability in Forming Current Sheets, ApJ **850**, 142 (2017), arXiv:1707.01862 [astro-ph.HE].

[31] D. A. Uzdensky and N. F. Loureiro, Magnetic reconnec-

tion onset via disruption of a forming current sheet by the tearing instability, Phys. Rev. Lett. **116**, 105003 (2016).

[32] W. Daughton, V. Roytershteyn, B. J. Albright, H. Karimabadi, L. Yin, and K. J. Bowers, Transition from collisional to kinetic regimes in large-scale reconnection layers, Phys. Rev. Lett. **103**, 065004 (2009).

[33] H. Ji and W. Daughton, Phase diagram for magnetic reconnection in heliophysical, astrophysical, and laboratory plasmas, Physics of Plasmas **18**, 111207 (2011), arXiv:1109.0756 [astro-ph.IM].

[34] L. Yang, H. Li, F. Guo, X. Li, S. Li, J. He, L. Zhang, and X. Feng, Fast Magnetic Reconnection with Turbulence in High Lundquist Number Limit, ApJL **901**, L22 (2020).

[35] F. Guo, X. Li, W. Daughton, H. Li, P. Kilian, Y.-H. Liu, Q. Zhang, and H. Zhang, Magnetic Energy Release, Plasma Dynamics, and Particle Acceleration in Relativistic Turbulent Magnetic Reconnection, ApJ **919**, 111 (2021), arXiv:2008.02743 [astro-ph.HE].

[36] H. Arnold, J. F. Drake, M. Swisdak, F. Guo, J. T. Dahlin, B. Chen, G. Fleishman, L. Glesener, E. Kontar, T. Phan, and C. Shen, Electron Acceleration during Macroscale Magnetic Reconnection, Phys. Rev. Lett. **126**, 135101 (2021), arXiv:2011.01147 [physics.plasm-ph].

[37] T. D. Phan, M. A. Shay, J. T. Gosling, M. Fujimoto, J. F. Drake, G. Paschmann, M. Øieroset, J. P. Eastwood, and V. Angelopoulos, Electron Bulk Heating in Magnetic Reconnection at Earth's Magnetopause: Dependence on the Inflow Alfvén Speed and Magnetic Shear, Geophys. Res. Lett. **40**, 4475 (2013).

[38] T. D. Phan, J. F. Drake, M. A. Shay, J. T. Gosling, G. Paschmann, J. P. Eastwood, M. Øieroset, M. Fujimoto, and V. Angelopoulos, Ion bulk heating in magnetic reconnection exhausts at earth's magnetopause: Dependence on the inflow alfvén speed and magnetic shear angle, Geophys. Res. Lett. **41**, 7002 (2014), 2014GL061547.

[39] Q. Zhang, J. F. Drake, and M. Swisdak, Particle Heating and Energy Partition in Low-$\beta$ Guide Field Reconnection with Kinetic Riemann Simulations, Phys. Plasmas **26**, 072115 (2019), arXiv:1904.12922 [physics.plasm-ph].

[40] Q. Zhang, J. F. Drake, and M. Swisdak, Instabilities and Turbulence in Low-$\beta$ Guide Field Reconnection Exhausts with Kinetic Riemann Simulations, Phys. Plasmas **26**, 102115 (2019), arXiv:1907.03181 [physics.plasm-ph].

[41] M. A. Shay, C. C. Haggerty, T. D. Phan, J. F. Drake, P. A. Cassak, P. Wu, M. Øieroset, M. Swisdak, and K. Malakit, Electron Heating during Magnetic Reconnection: A Simulation Scaling Study, Phys. Plasmas **21**, 122902 (2014).

[42] C. C. Haggerty, M. A. Shay, J. F. Drake, T. D. Phan, and C. T. McHugh, The competition of electron and ion heating during magnetic reconnection, Geophys. Res. Lett. **42**, 9657 (2015), 2015GL065961.

[43] F. Pedregosa, G. Varoquaux, A. Gramfort, V. Michel, B. Thirion, O. Grisel, M. Blondel, P. Prettenhofer, R. Weiss, V. Dubourg, J. Vanderplas, A. Passos, D. Cournapeau, M. Brucher, M. Perrot, and E. Duchesnay, Scikit-learn: Machine learning in Python, Journal of Machine Learning Research **12**, 2825 (2011).